

Highly Efficient Full van der Waals 1D p-Te/2D n-Bi₂O₂Se Heterodiodes with Nanoscale Ultra-Photosensitive Channels

Weijun Wang, You Meng, Wei Wang, Zhuomin Zhang, Pengshan Xie, Zhengxun Lai, Xiuming Bu, Yezhan Li, Chuntai Liu, Zengbao Yang, SenPo Yip, and Johnny C. Ho*

Continuous miniaturization of semiconductor devices is the key to boosting modern electronics development. However, this downscaling strategy has been rarely utilized in photoelectronics and photovoltaics. Here, in this work, a full-van der Waals (vdWs) 1D p-Te/2D n-Bi₂O₂Se heterodiode with a rationally designed nanoscale ultra-photosensitive channel is reported. Enabled by the dangling bond-free mixed-dimensional vdWs integration, the Te/Bi₂O₂Se type-II diodes show a high rectification ratio of 3.6×10^4 . Operating with 100 mV reverse bias or in a self-power mode, the photodiodes demonstrate excellent photo-detection performances, including high responsivities of 130 A W^{-1} (100 mV bias) and 768.8 mA W^{-1} (self-power mode), surpassing most of the reports of other heterostructures. More importantly, a superlinear photoelectric conversion phenomenon is uncovered in these nanoscale full-vdWs photodiodes, in which a model based on the in-gap trap-assisted recombination is proposed for this superlinearity. All these results provide valuable insights in light–matter interactions for further performance enhancement of photoelectronic devices.

1. Introduction

Enabled by the continuous rapid device miniaturization, semiconductor transistors have served as primary building blocks for the present-day information society in past several decades.^[1] However, unlike the miniaturization of traditional silicon-based field-effect transistors (FETs) in the large-scale integrated circuit, such device miniaturization strategy has been rarely utilized and studied in photoelectronics and photovoltaics.^[2] This consequence has restricted the further development of optoelectronic components for higher operation speed, better noise tolerance, and lower power consumption, thus impeding their massive integration.^[3] Therefore, in order to fulfill the downscaling requirements of optoelectronics,

all the critical factors governing the device functionality have to be carefully reformed, including materials, architectures, and concepts.^[4]

Although 2D/2D materials heterostructures have witnessed the downscaling of photosensitive channels ultimately to the nanoscale thickness, they may suffer from the poor light absorption efficiency and low responsivity due to the ultrathin nature of 2D materials.^[5] In contrast, the 1D/2D materials heterostructures show significant advantages, as they generally demonstrate non-degradation of light absorption powered by the antenna effects of nanowires (NWs).^[6] In addition, the reduced sensitive areas of devices would lead to an optimized resistance–capacitance time constant, which intrinsically promotes the response speed.^[2b,4,7]

On the other hand, most reported 1D/2D heterojunctions utilized the non-van der Waals (vdWs) semiconductor NWs, such as ZnO and Sb₂Se₃, in which the surface dangling bond inevitably give rise to the defect-induced performance degradation.^[8] Recently, elemental tellurium (Te) nanostructures, consisting of vdWs-bonded molecular chains, were found to possess the high current-carrying ability and high hole mobility $\approx 10^5 \text{ cm}^2 \text{ V}^{-1} \text{ s}^{-1}$. The unique DNA-like vdWs interactions together with excellent electrical performance endow Te NWs with great potential in constructing high-performance full-vdWs 1D/2D heterojunctions.^[9,10]

Here, we report a highly efficient full-vdWs 1D p-Te/2D n-Bi₂O₂Se heterodiode with the nanoscale ultra-photosensitive channel, illustrating a high rectification ratio of 3.6×10^4 . The strong interlayer coupling, dangling bond-free nature, and

W. Wang, Y. Meng, W. Wang, P. Xie, Z. Lai, X. Bu, Y. Li
Department of Materials Science and Engineering
City University of Hong Kong
Kowloon, Hong Kong SAR 999077, China


Z. Zhang, Z. Yang
Department of Mechanical Engineering
City University of Hong Kong
Kowloon, Hong Kong SAR 999077, China

C. Liu
Key Laboratory of Advanced Materials Processing & Mold
(Zhengzhou University)
Ministry of Education
Zhengzhou 450002, China

S. P. Yip, J. C. Ho
Institute for Materials Chemistry and Engineering
Kyushu University
Fukuoka 816-8580, Japan
E-mail: johnnyho@cityu.edu.hk

J. C. Ho
State Key Laboratory of Terahertz and Millimeter Waves
City University of Hong Kong
Kowloon, Hong Kong SAR 999077, China

J. C. Ho
Hong Kong Institute of Advanced Study
City University of Hong Kong
Kowloon, Hong Kong SAR 999077, China

 The ORCID identification number(s) for the author(s) of this article can be found under <https://doi.org/10.1002/adfm.202203003>.

DOI: 10.1002/adfm.202203003

enhanced charge transfer at the Te/Bi₂O₂Se junction interface are detailed studied by Raman spectroscopy, Kelvin probe force microscopy (KPFM), photoelectron spectroscopy, and electrical measurements. Under a reverse bias of 100 mV, the device exhibits a high responsivity (*R*) of 130 A W⁻¹, a large detectivity (*D*^{*}) of 2.5 × 10¹¹ Jones, and a fast response time down to 330 μs. Simultaneously, the well-aligned Type II heterojunctions endow self-powered photodetectors with a pronounced photovoltaic responsivity of 768.8 mA W⁻¹, a high light on/off ratio of 10⁴, and a fast response time of 400 μs. More importantly, a superlinear photoelectric conversion phenomenon is uncovered in our miniaturized full-vdWs photodiodes, with a model based on the in-gap trap-assisted recombination proposed for this superlinearity correspondingly. All these findings would provide valuable insights in light–matter interactions for further performance enhancement of photoelectronic devices.

2. Results and Discussion

Figure 1a schematically shows the diagram of Bi₂O₂Se nanosheets (NSs), and its tetragonal crystal structure is alternately stacked by [Bi₂O₂]_n²ⁿ⁺ and [Se]_n²ⁿ⁻ through the weak electrostatic interactions (Figure S1a, Supporting Information).^[11] In this work, Bi₂O₂Se NSs are synthesized by the chemical vapor deposition (CVD) method on mica (KMg₃AlSi₃O₁₀F₂) substrates. Detailed synthesis procedures can be found in the Methods section. Figure 1b and Figure S1b (Supporting Information) show a typical optical image (OM) and scanning electron microscope (SEM) image, respectively, which reveal good uniformity of the as-grown CVD Bi₂O₂Se NSs. We then carry out the X-ray photoelectron spectroscopy (XPS) survey to identify the chemical bonding states of Bi₂O₂Se NSs (Figure S2, Supporting Information). As depicted in Figure S2a (Sup-

porting Information), the peaks of Bi are centered at 163.6 and 158.3 eV, which corresponds to the binding energy of Bi 4f_{5/2} and Bi 4f_{7/2}, respectively. The O1s spectrum is resolved into two peaks at 529.2 and 531.4 eV (Figure S2b, Supporting Information), corresponding to the crystal lattice oxygen and surface absorbed oxygen, respectively. The spectrum of Se is resolved into two peaks, Se 3d_{5/2} and Se 3d_{3/2} with the binding energy of 52.4 and 53.2 eV, respectively (Figure S2c, Supporting Information). The XPS analysis shows that the as-grown Bi₂O₂Se NSs are in high quality and consistent with the previous reports.^[12] The single-crystalline nature of the as-grown Bi₂O₂Se NSs and its tetragonal I4/mmm space group were confirmed by X-ray diffraction (XRD) pattern (Figure S3a, Supporting Information), and the lattice planes indexed as (002), (004), and (006) agree well with a reference diffractogram indicating the pure phase of layered Bi₂O₂Se.^[13] The high-resolution transmission electron microscopy (HRTEM) characterization of Bi₂O₂Se NSs suggests that the d-spacings of (110) planes are 0.27 nm, while its single-crystal nature is confirmed by the inset SAED pattern (Figure 1c). The above characterizations clearly confirm that the Bi₂O₂Se NSs synthesized here are of high quality.

At the same time, as depicted in Figure 1d, Te NWs are composed of covalently bonded atoms sequenced in a helical chain along a single axis, with chains packed in a hexagonal array via vdWs forces (Figure S1c, Supporting Information).^[14] Similar to the synthesis of CVD-grown Bi₂O₂Se NSs, Te NWs synthesized by CVD method^[10,15] show an excellent uniformity in diameters and lengths, as displayed in Figure 1e and Figure S1d (Supporting Information). The structure of the as-grown Te NWs has been confirmed by X-ray diffraction (XRD) (Figure S3b, Supporting Information). Two sharp diffraction peaks can be indexed to the (001) and (002) crystal planes (PDF#36-1452), indicating the high-quality growth of the trigonal Te NW crystals. To determine the atomic structure and crystallinity of the

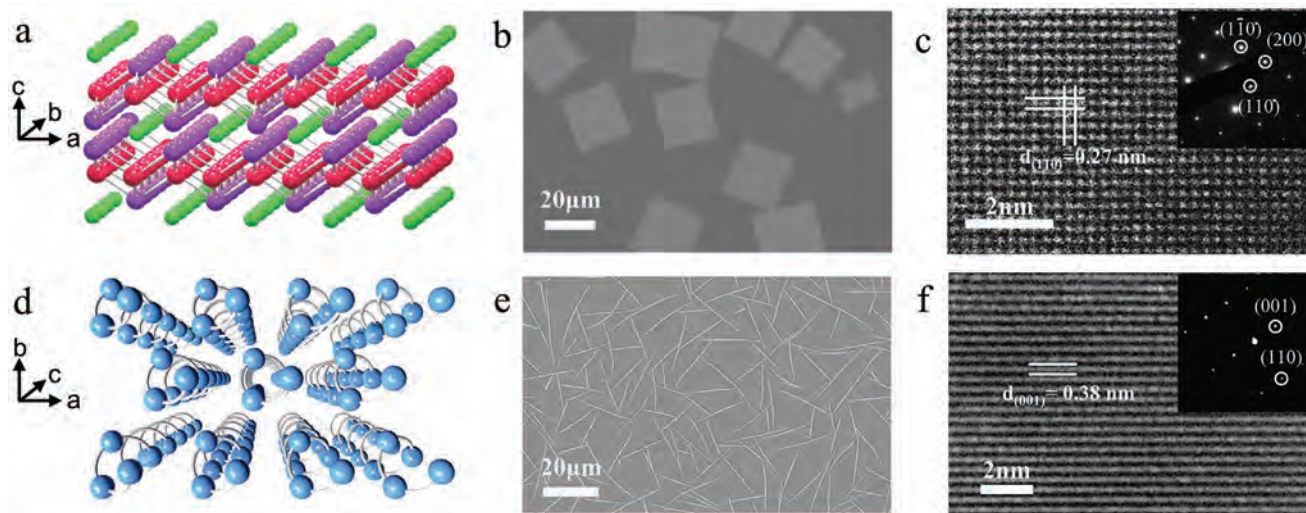


Figure 1. a) Illustration of the crystal structure of Bi₂O₂Se nanosheets (NSs). b) SEM image of the as-grown Bi₂O₂Se NSs on mica synthesized by the CVD method. c) HRTEM image of Bi₂O₂Se NSs, indicating the d-spacings of 0.27 nm for (110) planes. The inset SAED pattern of Bi₂O₂Se NSs suggests its single crystallinity. d) Illustration of the crystal structure of Te NWs with helical atomic chains. e) SEM image of the uniform Te NWs grown on mica via the CVD method. f) HRTEM characterization of the Te NWs shows an interplanar spacing distance of 0.38 nm, corresponding to the lattice spacing of (001) planes. Its single crystallinity is confirmed by the inset SAED image.

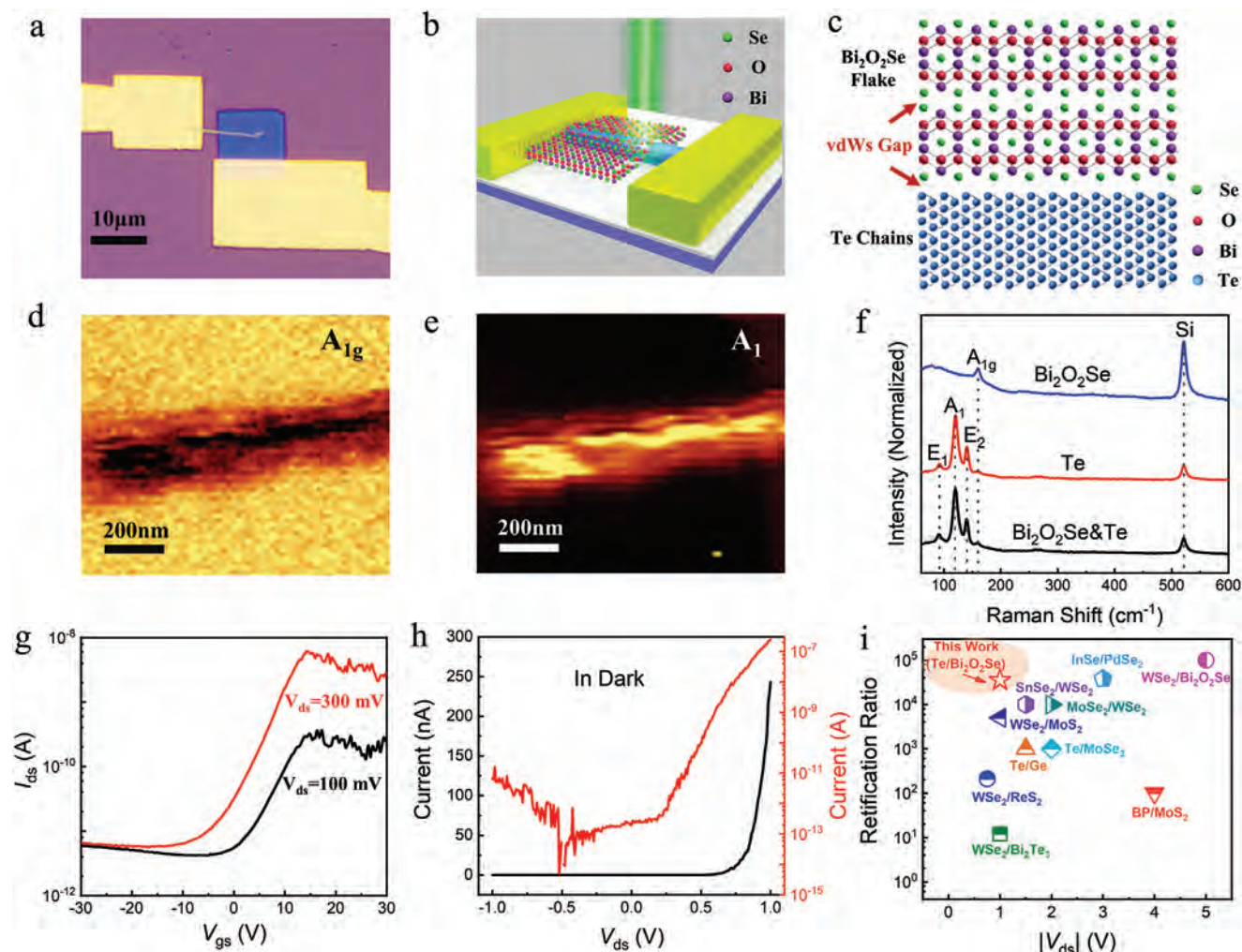


Figure 2. a) OM image and b) schematic diagram of the full-vdWs 1D Te/2D Bi₂O₂Se heterojunction device. The Bi₂O₂Se NS is stacked on top of the Te NW. c) Schematic diagram of the cross-sectional vdWs heterojunction region. d) Raman mapping of the A_{1g} peak of Bi₂O₂Se and e) the A₁ peak of Te in the overlapped heterojunction region. f) Raman spectra of pure Te, Bi₂O₂Se, and their heterojunction region. f) Raman spectra of pure Te, Bi₂O₂Se, and their heterojunction region. g) Transfer characteristics of the device at distinct biases of 100 and 300 mV, respectively. h) I_{ds} - V_{ds} curves of the Te/Bi₂O₂Se device on linear and logarithmic scales in the bias range of -1 to 1 V with zero gate voltage in the dark. i) RF of Te/Bi₂O₂Se heterojunction photodetector under a small bias of $|V_{ds}| = 1$ V, and performance comparison with the state-of-the-art 2D materials heterojunctions.

Te NWs, HRTEM is performed (Figure 1f). The HRTEM image of Te NWs shows the interplanar spacing distances of around 0.2 nm, being consistent with the lattice spacing of (001) planes of hexagonal Te crystals.^[16] Combined with the inset SEAD pattern, the excellent single crystallinity of Te NWs is obtained.

After the individual 1D Te NWs and 2D Bi₂O₂Se NSs have been fabricated, the full-vdWs Te/Bi₂O₂Se heterojunction devices are then constructed on SiO₂/Si substrates using a standard photolithography process with Au (50 nm) electrodes. Before constructing the Te/Bi₂O₂Se heterojunction, we conducted Raman spectroscopy, which showed the high uniformity and high quality of the transferred materials on SiO₂/Si (Figure S4, Supporting Information). **Figure 2a** presents the OM image of the fabricated device, while **Figure 2b** shows the schematic diagram of the corresponding device. In the heterojunction region, single helical chains of the Te NW are bonded

by the weak vdWs force, and the interfacial atomic chains of Te NW are strongly coupled with the Bi₂O₂Se NS through vdWs interaction with a narrow vdWs gap as schematically demonstrated in **Figure 2c**. To confirm the coupling effect and charge transfer phenomenon at the Te/Bi₂O₂Se heterojunction interface, we further conduct the optical measurements across the heterojunction region.^[17] The Raman spectra of pure Te, Bi₂O₂Se, and the overlapped heterojunction are respectively presented in **Figure 2f**. Three distinctive peaks of Te NWs are observed, including the most substantial Raman peak located at ≈ 121 cm⁻¹. This peak is associated with the A₁ mode, corresponding to the chain-expansion vibration of Te atoms along the basal plane. The other two peaks of E₁ mode (93 cm⁻¹) and E₂ (141 cm⁻¹) are observed, corresponding to the asymmetric bond-stretching along the *c*-axis and predominate bond-bending and bond-stretching types, respectively. In

contrast, the vibration mode of Bi₂O₂Se located at ≈ 160 cm⁻¹ is assigned to A_{1g} Raman peak. The Raman mappings of Bi₂O₂Se A_{1g} mode (Figure 2d) and Te A₁ mode (Figure 2e) further confirm the high crystallinity and excellent homogeneity of each component. There is no noticeable shift for all the characteristic peaks in the overlapped heterojunction region, confirming the high quality of the vdWs heterojunction obtained after the wet transfer processes.^[18] Apparently, the drastic Raman intensity reduction of A_{1g} mode of Bi₂O₂Se is witnessed at the junction region, which is known as “Raman quenching,” indicating a strong interfacial coupling between the Te NWs and the Bi₂O₂Se NSs of our heterojunction devices.^[19]

In general, it has been widely reported that Te is p-type^[10] semiconductor, whereas Bi₂O₂Se is an n-type material.^[17] This way, when the Bi₂O₂Se NS is stacked on top of the Te NW, a type II staggered vdWs p-n junction is usually formed with the carrier transport showing antiambipolar-like characteristics.^[20] Specifically, as the gate voltage is swept from -30 to 30 V, the transfer characteristics of our Te/Bi₂O₂Se heterodiode could be divided into three regions (Figure 2g), prominently dictated by the gate-tuned conductivities of Te and Bi₂O₂Se. In region I ($V_{gs} < -10$ V), the Bi₂O₂Se channel is completely depleted, and thus the entire channel is shut down, leading to the lowest I_{ds} . In region II (-10 V $< V_{gs} < 15$ V), the Bi₂O₂Se channel begins to be turned on, resulting in a continuous increase in the channel current until the heterodiode is completely turned on. In region III ($V_{gs} > 15$ V), the drain current merely begins to slightly decrease, since the Te channel cannot be effectively depleted due to its ultrahigh hole concentration originated from the narrow bandgap.^[21] Notably, Figure 2h presents the current-voltage (I - V) curves of Te/Bi₂O₂Se heterojunction in linear (black) and logarithmic (red) scale with the source/drain bias range of -1 to 1 V with zero gate voltage in the dark. This device shows a strong rectification behavior, with a calculated ideality factor of 1.9 based on the diffusion theory of Shockley.^[22] The rectification factor (RF) can reach up to 3.6×10^4 under a small bias of $|V_{ds}| = 1$ V, being superior to most vdWs 2D heterostructures reported in recent literatures (Figure 2i).^[23]

Benefiting from the excellent rectification behavior and ultralow reverse current (10^{-12} A), we further explore the photoelectronic properties of the Te/Bi₂O₂Se heterojunction without gate voltage. The I_{ds} - V_{ds} curves on a logarithmic scale under different light intensities of 635, 532, and 405 nm are demonstrated in Figure 3a and Figure S6 (Supporting Information), respectively, with their corresponding linear-scale plots depicted in Figure S7 (Supporting Information). When a low reverse bias ($V_{ds} = -100$ mV) is applied in the dark, the device would work in off-state with an ultralow reverse current. Whereas, under light irradiation, the photogenerated carriers (electrons and holes) can be effectively separated and transferred into distinct materials at the interface due to the enhanced interface potential barrier. Thus, a maximum on/off current ratio of 4.7×10^4 (635 nm), 1.1×10^5 (532 nm), and 1.6×10^4 (405 nm) can be respectively achieved at a small negative bias (-100 mV). The photoswitching characteristics show that the photocurrent response continuously increases as the light intensity increases (Figure 3b and Figure S8, Supporting Information), which is consistent with the fact that the number of photogenerated carriers is proportional to the incoming photon flux.^[31]

Furthermore, we also measure the time-resolved photoreponse of the Te/Bi₂O₂Se heterojunction under different laser wavelengths, where the device exhibits a fast response speed of several hundred microseconds (Figure 3c and Figure S9, Supporting Information). In particular, the device yields a fast rise time of 330 μ s and a decay time of 430 μ s under an illumination intensity of 251.5 mW cm⁻² at 532 nm laser.

To shed light into the photocurrent generation mechanism, we further studied the light intensity-dependent photocurrent under different laser wavelengths. As presented in Figure 3d, the photocurrent increases sub-linearly with the excitation powers. The photocurrent displays a strong dependence on the power intensity, in which the experimental data can be fitted well by the following relationship of $I_{ph} \propto P^\alpha$, where α is the power exponent that is usually used to explain the photocurrent generation mechanism. Briefly, when $\alpha = 1$, the photocurrent is dominated by the photoconductive effect. When $\alpha = 0$, the photocurrent is dictated by the photogating effect involving trap states.^[32] By fitting the experimental data under different laser wavelengths, the individual power exponent (α) can be extracted accordingly. All the extracted α values are smaller than 1, indicating the recombination kinetics of photogenerated carriers and trap states.^[17,33] In order to evaluate the photodetection performance of the device, the responsivity (R) and specific detectivity (D^*) are calculated. The R value can be calculated by the equation of $R = I_{ph}/(PS)$, where I_{ph} , P , and S are the photocurrent, incident power density, and functional areas of the device, respectively. D^* can be expressed as $D^* = RS^{1/2}/(2eI_{dark})^{1/2}$, where I_{dark} represents the dark current. Figure 3e,f demonstrate the extracted R and D^* under different incident light intensities at different excitation wavelengths of 635, 532, and 405 nm, respectively. Both R and D^* decrease with the increasing light intensity. It is understandable that as the photogenerated electrons are captured by the trap states under lower power intensity, a drop in the recombination possibility is resulted.^[34] The maximum R and D^* values are found to be 130 A W⁻¹ and 2.5×10^{11} Jones, correspondingly, which reveal its superior responsivity and detectivity compared to the typical state-of-the-art low-dimensional semiconductor-based photodetectors (Figure 3g). In addition, although a small bias ($V_{ds} = -100$ mV) is applied, the full-vdWs Te/Bi₂O₂Se heterodiode shows a significantly improved response speed (rise/decay time) down to 330/430 μ s, surpassing many previously reported literature (Figure 3h). This enhancement can be attributed to the strongly coupled dangling-bond-free junction interface, which facilitates the effective separation and transfer of photogenerated carriers.^[22,35] Overall, its performance is already better than many advanced nanomaterials-based photodetectors, suggesting its great promise in high-speed switching, low-noise detection, and low-power consumption devices.

Moreover, as the carrier transport behavior of the heterojunction is intrinsically determined by the band alignment,^[36] it is necessary to assess the energy band alignment of the heterojunction. Prior to this, the surface morphology of the heterojunction is characterized by the atomic force microscope (AFM), indicating that the diameter of the Te NW is ≈ 210 nm and the thickness of the Bi₂O₂Se NS is ≈ 9.8 nm (≈ 15 layers) (Figure 4a). Typically, NWs with a small diameter of 100–300 nm would allow a nanowire cavity to interact with

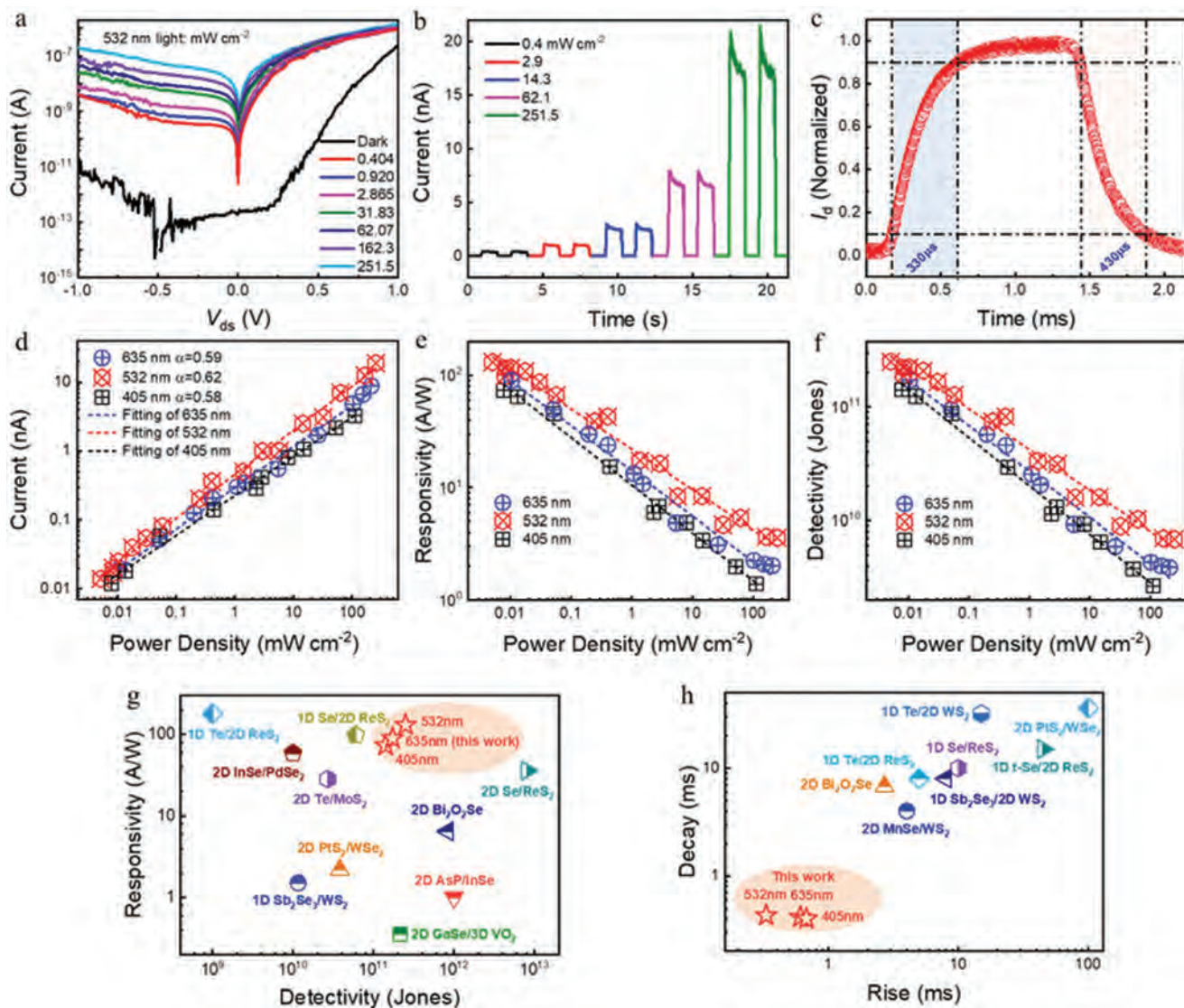


Figure 3. a) Logarithmic-scale I_{ds} - V_{ds} curves as a function of incident power densities measured in the dark and under 532 nm light. b) Photoswitching characteristics measured at $V_{ds} = -100$ mV under 532 nm laser with different light power densities. c) Time-resolved photoresponse shows fast photoswitching characteristics measured at $V_{ds} = -100$ mV under 532 nm. d) Photocurrent dependence of laser power intensity at $V_{ds} = -100$ mV under different visible light wavelengths of 635, 532, and 405 nm, respectively. e) Responsivity and f) detectivity of the device under varying light intensities at $V_{ds} = -100$ mV under laser illumination of 635, 532, and 405 nm, respectively. g) Responsivity, detectivity, and h) rise and decay time of typical state-of-the-art low-dimensional semiconductor-based photodetectors reported in literature including Te/ReS₂,^[10] Sb₂Se₃/WS₂,^[8b] AsP/InSe,^[19b] InSe/PdSe₂,^[22] GaSe/VO₂,^[24] Te/MoS₂,^[25] MnSe/WS₂,^[26] Bi₂O₂Se,^[27] Se/ReS₂,^[28] PtS₂/WSe₂,^[29] and Te/WS₂.^[30]

incident light beyond its projected incident area, resulting in the extended absorption and scattering cross-sections at desired wavelengths (a large refractive index contrast for strong light confinement).^[37] In addition, the sub-10 nm thickness of Bi₂O₂Se has been featured with excellent electron mobility at room temperature and the external quantum efficiency up to 230 cm² V⁻¹ s⁻¹ and 1.5 × 10⁷%, respectively.^[38] According to the previous study, with rationally designed diameter/thickness, Te NWs combined with Bi₂O₂Se NSs in this work would produce a relatively high light absorption efficiency, which is suitable for photoelectronic applications.^[21,27,39] Thus, we then carry out the Kelvin probe force microscopy (KPFM) measurement to reveal the Fermi level shift and determine the energy band alignment

(Figure 4b). The contact potential difference (CPD) between the probe and the sample is calculated by

$$V_{CPD} = \frac{W_{Tip} - W_{Sample}}{e} \quad (1)$$

where W_{Tip} and W_{Sample} are the work function of the tip and the sample, respectively. The work function difference between Te NW and Bi₂O₂Se NS can be obtained by acquiring the V_{CPD} difference. According to the sectional profile of V_{CPD} , the V_{CPD} difference of the Te/Bi₂O₂Se heterojunction is calculated to be around 30 mV (Figure 4c). In addition, as characterized by ultraviolet photoelectron spectroscopy (UPS) of Bi₂O₂Se NSs

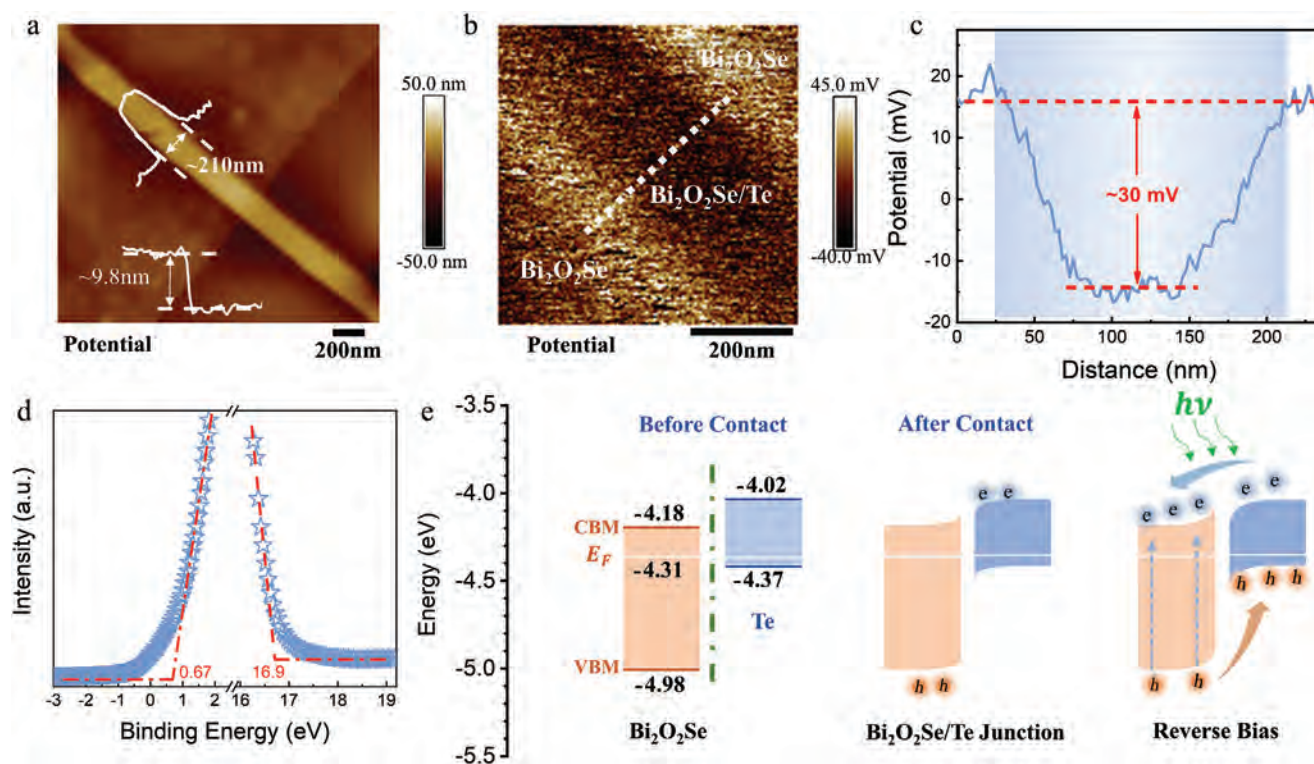


Figure 4. a) AFM topological morphology of the Te/Bi₂O₂Se heterojunction. The height profiles of the Te NW and the Bi₂O₂Se NS are shown in the inset. b) KPFM image of the Te/Bi₂O₂Se heterojunction. c) KPFM profile obtained along with the white dashed line in (b). d) Ultraviolet photoelectron spectrum (UPS) of Bi₂O₂Se NSs for the evaluation of work function and valence band edge. e) Schematic of the band diagram of the Te/Bi₂O₂Se heterojunction (I) before contact, (II) after contact, and (III) at reverse bias when illuminated.

(Figure 4d), the work function (W) of Bi₂O₂Se is calculated as 4.3 eV by subtracting the second electron cut-off edge (16.9 eV) from the photon energy of the He I light source (21.21 eV). The valance band energy of the Bi₂O₂Se is determined to be 0.67 eV. Combining the above analysis and further taking the bandgap of thin Bi₂O₂Se NSs and Te NWs to be 0.8 eV^[32b,40] and 0.35 eV, respectively,^[35,41] we construct a type II band alignment before contact in Figure 4e(I). When the two materials contact, the higher Fermi level of Bi₂O₂Se induces electrons transfer to Te until reaching a thermal equilibrium state with an identical E_F . The leaving holes and electrons would accumulate at the Bi₂O₂Se and Te side, accordingly, leading to the energy bands of Bi₂O₂Se sloping upwards toward the Te side and forming a built-in potential from Bi₂O₂Se to Te side across the junction (Figure 4e(II)). When applying a negative bias, the direction of the external electric field is identical to its built-in potential (Figure 4e(III)). The enhanced potential difference under a small bias can further promote the photoexcited electron-hole pairs separation, contributing to the photoconductivity-dominant responsivity mechanism.^[5b]

More importantly, these heterojunction devices can also be operated as self-powered photodetectors with zero bias by using the photovoltaic effect. Without consuming external power, these devices are expected to become more reliable, meeting the requirements of energy-conserving photoelectronics for the low-carbon era. After systematically exploring the photoconductive effect of the heterojunction under a small bias, we then investigate their photovoltaic properties. Figure 5a shows

the time-resolved photovoltaic response under 532 nm illumination of various power intensities. It is evident that the photocurrent exhibits a remarkable and fast switching with a high on/off current ratio of 10^4 and a fast response speed of ≈ 400 μ s under zero bias (Figure 5b), attributable to the strongly coupled dangling-bond-free vdWs junction interface. To assess the photocurrent generation mechanism behind the photovoltaic mode, the photocurrent dependence of power intensities is fitted by the power law function of $I_{ph} \propto P^\alpha$. As shown in Figure 5c, the device shows two distinct power exponents (α) at different power intensities. At a high power intensity larger than 4 $mW\ cm^{-2}$, the power exponent of α is smaller than 1, yielding a sub-linear behavior. The sub-linear behavior is mainly resulted from the reduced recombination probability of photogenerated carriers due to the trap states causing the responsivity decline.^[42] The photocurrent exhibits a superlinear dependence on power intensity less than 4 $mW\ cm^{-2}$, which is rarely observed and will be explained more in detail below.

To obtain a deeper insight into the physical mechanism behind the superlinearity, a possible mechanism based on trap-assisted recombination is proposed.^[52] Due to the small energy gap of Te (0.35 eV), any trap levels must lie close enough to a band edge, which substantially reduces its effectiveness in recombination.^[53] Thus, to simplify the model, we do not consider the trap level of Te in the vdWs heterojunctions, merely focusing on the in-gap trapping levels in Bi₂O₂Se. As shown in Figure 5d, three types of recombination centers (RCs) with different energies and capture cross-sections in Bi₂O₂Se are located near the valence (RC1),

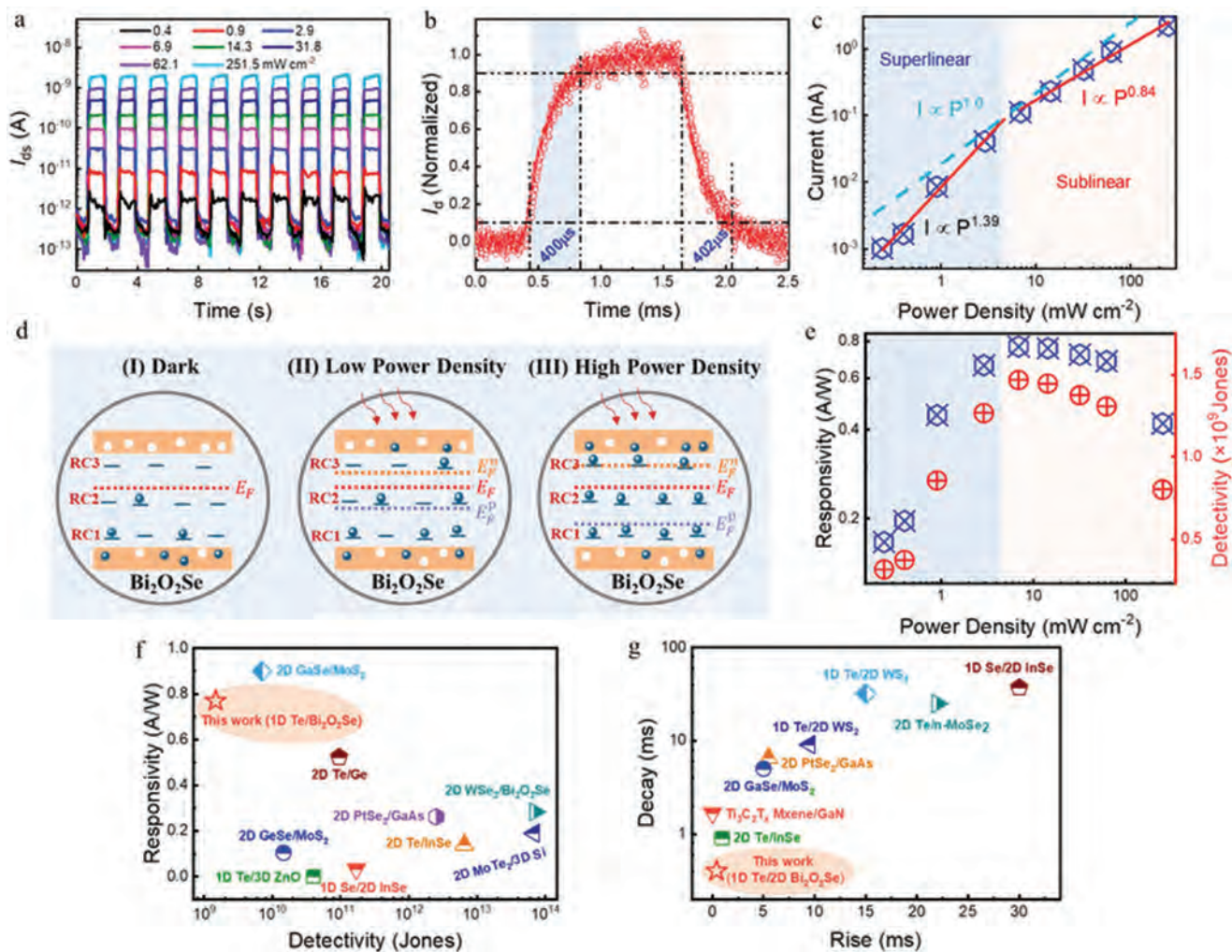


Figure 5. a) Photovoltaic photoswitching characteristics of the heterojunction under 532 nm laser with different light power densities. b) Time-resolved photoresponse, and c) photocurrent dependence of laser power intensity in the photovoltaic mode under 532 nm laser. d) Schematics of the bandgap model to explain the superlinear behavior of power-dependent photocurrent. Three distinct types of recombination centers (RCs) under dark (left), low-power density (middle), and high-power density (right) are presented, respectively. E_F is the Fermi level, E_F^e and E_F^h are the quasi-Fermi levels of electrons and holes under illumination, respectively. e) Corresponding responsivity and detectivity of the device under varying light intensities. f) Photovoltaic responsivity, detectivity, and h) rise and decay time of typical state-of-the-art low-dimensional semiconductor-based photodetectors reported in literature such as GaSe/MoS₂,^[43] Te/Ge,^[44] PtSe₂/GaAs,^[34] WSe₂/Bi₂O₃Se,^[17] GeSe/MoS₂,^[43] Te/InSe,^[45] MoTe₂/Si,^[46] Te/ZnO,^[47] Se/InSe,^[48] Ti₃C₂T_x Mxene/GaN,^[49] PtSe₂/GaAs,^[34] Te/WS₂,^[30] Te/MoSe₂,^[50] and Se/InSe.^[51]

middle (RC2), and conduction band (RC3), respectively. Recombination centers of type 1 (RC1) have a high hole capture but a low electron capture cross-section, while RC2 and RC3 are considered to have high capture cross-sections for both electrons and holes. In the dark, the Fermi level (E_F) is located above RC1 and RC2, but below RC3 (Figure 5d(I)). As exposed to light, the concentration of photogenerated carriers (electrons and holes) increases, leading to the Quasi-Fermi levels of E_F^e and E_F^h shifting closer to the valence and conduction band edges, respectively. This means that RC1 and RC2 are almost occupied at low power density, while RC3 is almost empty, dominating the ultimate recombination rate (Figure 5d(II)). With the increasing light intensity, the occupancy of RC3 increases, while RC2 becomes partly empty, and the recombination traffic is mostly through RC2. As the power intensity further increases, the occupation

of RC1, RC2, and RC3 becomes comparable (Figure 5d(III)), resulting in a significant drop in the recombination rate, leading to a superlinear photocurrent.

Based on the above analysis, this superlinearity is closely related to the intrinsic material defects that would induce the in-gap RCs. This property is rarely observed because the surface-induced states may lead to the onset of the sublinearity. However, due to the atomically sharp and dangling-bonds-free interface of the Te/Bi₂O₃Se heterodiode, the superlinearity is well observed as the surface-induced states are effectively suppressed. Moreover, the device shows a pronounced photovoltaic responsivity of 768.8 mA W⁻¹ and a high detectivity of 1.5×10^9 Jones at the intensity of 6.9 mW cm⁻² (Figure 5e). To benchmark the performance of the device with previously reported literature, comparisons of the critical figure of merits, R and D^* , and response

speeds are presented in Figure 5f,g, respectively. Overall, the heterodiode performs significantly better than many previously reported vdWs heterostructure photodetectors, highlighting its great potential in photovoltaic applications.

3. Conclusion

In summary, we explore the device miniaturization strategy to fabricate full-vdWs Te/Bi₂O₂Se heterodiodes with nanoscale ultra-photosensitive channels. The strong interlayer coupling, dangling bond-free nature, and efficient charge transfer between Te and Bi₂O₂Se provide a high rectification ratio up to 3.6×10^4 and an ultralow reverse dark current of sub-pA level. Under a small reverse bias of 100 mV, the device exhibits high responsivity, detectivity, and response time of 130 A W⁻¹, 2.5×10^{11} Jones and 330 μs, respectively. Moreover, the self-powered photodetection shows a pronounced photovoltaic responsivity of 768.8 mA W⁻¹, a high on/off current ratio of 10⁴, and a high-speed response time of 400 μs, accordingly. It is also noted that the superlinear photocurrent dependence on light intensity is observed, and a simplified model is proposed to explain its origin based on the in-gap trap-assisted recombination. These outstanding characteristics highlight the great potential of full-vdWs 1D p-Te/2D n-Bi₂O₂Se heterodiodes in future optoelectronics with high sensitivity, fast photoresponse, and low-power consumption.

4. Experimental Section

Methods: Similar to the previous literature, Bi₂O₂Se NSs and Te NWs were synthesized by the CVD method.^[10,11] Briefly, Mica substrates were placed 10–12 cm downstream, while the power of Bi₂Se₃ (Aldrich, 99.99%) and Bi₂O₃ (Thermo Fisher, 98%) in two quartz boats were put on the upstream and the center of the furnace, respectively. The furnace was set to 630–650 °C with a ramping time of 15 min and a hold time of 10–20 min at about 200 torr. The synthesis of Te NWs was similar to that of Bi₂O₂Se NSs but grown in ambient pressure with Si substrates. The precursor of Te powders (Aldrich, 99.999%) was positioned in the center of the furnace (440–490 °C), while silicon substrates were placed downstream. Before the heating process, both systems were thoroughly flushed by high-purity argon gas (300 sccm) for 20 min to drive the moisture and oxygen out. After growth, the two systems were quickly cooled to room temperature.

Device Fabrication: Firstly, the processed growth substrate was put into anhydrous ethanol and underwent minor ultrasonication to obtain a uniform NW colloidal suspension. Then, the NWs were drop-casted onto SiO₂/Si (270 nm thick thermal oxide) substrates. The as-grown Bi₂O₂Se NSs were next detached from mica to deionized water by a PMMA-assisted wet transfer method^[54] and further transferred to the top of Te NW on the SiO₂/Si substrate with the aid of a 2D multifunctional micromanipulation transfer system. After drying and removing PMMA in acetone, the source/drain regions of Bi₂O₂Se/Te heterojunction were patterned by standard electron-beam lithography, followed by thermal evaporation of 50 nm thick Au electrodes and a lift-off process.

Characterization: The surface morphologies of the materials were characterized by optical microscope, scanning electron microscope (XL30, FEI/Philips ESEM-FEG), and atomic force microscope (Dimension Icon, Bruker), respectively. The Raman spectra were collected by a confocal microscope spectrometer (Alpha 300R, WITec), and the energy band alignment was measured by a UPS technique

(Axis Ultra DLD, Kratos). The corresponding crystal structures and crystallinity were examined by analyzing the X-ray diffraction pattern and imaging with HRTEM (Tecnai G2 F30, FEI). The electronic and photodetection performance of the Te/Bi₂O₂Se heterojunction was measured by a semiconductor analyzer (Agilent 4155C) and probe station under different laser sources (635, 532, and 405 nm), whose power intensity were calibrated by a power meter (PM400, Thorlabs). Time-resolved photoresponse curves of the heterojunction were measured by a digital oscilloscope (TBS 1102B-EDU, Tektronix) coupled with a low-noise current preamplifier (SR570, Stanford Research Systems).

Supporting Information

Supporting Information is available from the Wiley Online Library or from the author.

Acknowledgements

W.W.J. and M.Y. contributed equally to this work. This work was financially supported by a fellowship award from the Research Grants Council of the Hong Kong Special Administrative Region, China (CityU RFS2021-1S04), Shenzhen Municipality Science and Technology Innovation Commission (Grant No. SGDX2020110309300402; “Modulation and Detection of Terahertz Waves based on Semi-Metallic Two-Dimensional Materials,” CityU), and Foshan Innovative and Entrepreneurial Research Team Program (No. 2018IT100031).

Conflict of Interest

The authors declare no conflict of interest.

Data Availability Statement

The data that support the findings of this study are available from the corresponding author upon reasonable request.

Keywords

heterodiode, self-powered photodetection, superlinearity, Te/Bi₂O₂Se

Received: March 16, 2022

Revised: April 4, 2022

Published online: May 6, 2022

- [1] a) M. Casalino, G. Coppola, R. M. D. L. Rue, D. F. Logan, *Laser Photonics Rev.* **2016**, *10*, 895; b) S. Y. Liang, H. Xia, *Opt. Lett.* **2021**, *46*, 6075.
- [2] a) P. Q. Wang, X. F. Duan, *MRS Bull.* **2021**, *46*, 534; b) I. M. Asuo, P. Fourmont, I. Ka, D. Gedamu, S. Bouzidi, A. Pignolet, R. Nechache, S. G. Cloutier, *Small* **2019**, *15*, 1804150.
- [3] a) E. Kamrani, F. Lesage, M. Sawan, *IEEE Sens. J.* **2014**, *14*, 258; b) J. Lee, B.-S. Choi, D. Seong, J. Lee, S.-H. Kim, J. Lee, J.-K. Shin, P. Choi, *J. Sens. Sci. Technol.* **2018**, *27*, 362.
- [4] F. F. Ren, K. W. Ang, J. D. Ye, M. B. Yu, G. Q. Lo, D. L. Kwong, *Nano Lett.* **2011**, *11*, 1289.
- [5] a) F. Wu, Q. Li, P. Wang, H. Xia, Z. Wang, Y. Wang, M. Luo, L. Chen, F. S. Chen, J. S. Miao, X. S. Chen, W. Lu, C. X. Shan, A. L. Pan,

- X. Wu, W. C. Ren, D. Jariwala, W. D. Hu, *Nat. Commun.* **2019**, *10*, 4663; b) Y. M. Ma, B. W. Dong, J. X. Wei, Y. H. Chang, L. Huang, K. W. Ang, C. Lee, *Adv. Opt. Mater.* **2020**, *8*, 2000337.
- [6] a) G. Chen, J. Wu, Q. J. Lu, H. R. H. Gutierrez, Q. Xiong, M. E. Pellen, J. S. Petko, D. H. Werner, P. C. Eklund, *Nano Lett.* **2008**, *8*, 1341; b) S. K. Kim, X. Zhang, D. J. Hill, K. D. Song, J. S. Park, H. G. Park, J. F. Cahoon, *Nano Lett.* **2015**, *15*, 753.
- [7] M. Casalino, M. Iodice, L. Sirlito, I. Rendina, G. Coppola, *Opt. Express* **2013**, *21*, 28072.
- [8] a) Y. T. Lee, P. J. Jeon, J. H. Han, J. Ahn, H. S. Lee, J. Y. Lim, W. K. Choi, J. D. Song, M. C. Park, S. Im, D. K. Hwang, *Adv. Funct. Mater.* **2017**, *27*, 1703822; b) G. Sun, B. Li, J. Li, Z. Zhang, H. Ma, P. Chen, B. Zhao, R. Wu, W. Dang, X. Yang, *Nano Res.* **2019**, *12*, 1139.
- [9] G. Qiu, C. Niu, Y. X. Wang, M. W. Si, Z. C. Zhang, W. Z. Wu, P. D. D. Ye, *Nat. Nanotechnol.* **2020**, *15*, 585.
- [10] J. J. Tao, J. B. Jiang, S. N. Zhao, Y. Zhang, X. X. Li, X. S. Fang, P. Wang, W. D. Hu, Y. H. Lee, H. L. Lu, D. W. Zhang, *ACS Nano* **2021**, *15*, 3241.
- [11] U. Khan, Y. T. Luo, L. Tang, C. J. Teng, J. M. Liu, B. L. Liu, H. M. Cheng, *Adv. Funct. Mater.* **2019**, *29*, 1807979.
- [12] D. Ding, Z. Jiang, D. Ji, N. V. Myung, L. Zan, *Chem. Eng. J.* **2020**, *400*, 125931.
- [13] J. Wu, H. Yuan, M. Meng, C. Chen, Y. Sun, Z. Chen, W. Dang, C. Tan, Y. Liu, J. Yin, *Nat. Nanotechnol.* **2017**, *12*, 530.
- [14] C. S. Zhao, C. L. Tan, D. H. Lien, X. H. Song, M. Amani, M. Hettick, H. Y. Y. Nyein, Z. Yuan, L. Li, M. C. Scott, A. Javey, *Nat. Nanotechnol.* **2020**, *15*, 53.
- [15] Z. Shi, R. Cao, K. Khan, A. K. Tareen, X. S. Liu, W. Y. Liang, Y. Zhang, C. Y. Ma, Z. N. Guo, X. L. Luo, H. Zhang, *Nano-Micro Lett.* **2020**, *12*, 99.
- [16] M. Peng, R. Z. Xie, Z. Wang, P. Wang, F. Wang, H. N. Ge, Y. Wang, F. Zhong, P. S. Wu, J. F. Ye, Q. Li, L. L. Zhang, X. Ge, Y. Ye, Y. C. Lei, W. Jiang, Z. G. Hu, F. Wu, X. H. Zhou, J. S. Miao, J. L. Wang, H. G. Yan, C. X. Shan, J. N. Dai, C. Q. Chen, X. S. Chen, W. Lu, W. D. Hu, *Sci. Adv.* **2021**, *7*, eabf7358.
- [17] P. Luo, F. K. Wang, J. Y. Qu, K. L. Liu, X. Z. Hu, K. W. Liu, T. Y. Zhai, *Adv. Funct. Mater.* **2021**, *1*, 31.
- [18] Y. X. Deng, Z. Luo, N. J. Conrad, H. Liu, Y. J. Gong, S. Najmaei, P. M. Ajayan, J. Lou, X. F. Xu, P. D. Ye, *ACS Nano* **2014**, *8*, 8292.
- [19] a) X. Zhou, X. Z. Hu, S. S. Zhou, H. Y. Song, Q. Zhang, L. J. Pi, L. Li, H. Q. Li, J. T. Lu, T. Y. Zhai, *Adv. Mater.* **2018**, *30*, 1703286; b) F. Wu, H. Xia, H. D. Sun, J. W. Zhang, F. Gong, Z. Wang, L. Chen, P. Wang, M. S. Long, X. Wu, J. L. Wang, W. C. Ren, X. S. Chen, W. Lu, W. D. Hu, *Adv. Funct. Mater.* **2019**, *29*, 1900314.
- [20] R. X. Hu, E. X. Wu, Y. Xie, J. Liu, *Appl. Phys. Lett.* **2019**, *115*, 073104.
- [21] P. Dasika, D. Samantaray, K. Murali, N. Abraham, K. Watanabe, T. Taniguchi, N. Ravishankar, K. Majumdar, *Adv. Funct. Mater.* **2021**, *31*, 2006278.
- [22] W. Ahmad, J. D. Liu, J. Z. Jiang, Q. Y. Hao, D. Wu, Y. X. Ke, H. B. Gan, V. Laxmi, Z. B. Ouyang, F. P. Ouyang, Z. Wang, F. Liu, D. A. Y. Qi, W. J. Zhang, *Adv. Funct. Mater.* **2021**, *31*, 2104143.
- [23] H. W. Liu, X. L. Zhu, X. X. Sun, C. G. Zhu, W. Huang, X. H. Zhang, B. Y. Zheng, Z. X. Lou, Z. Y. Luo, X. Wang, D. Li, A. L. Pan, *ACS Nano* **2019**, *13*, 13573.
- [24] J. Y. Zhou, M. Z. Xie, H. Ji, A. Y. Cui, Y. Ye, K. Jiang, L. Y. Shang, J. Z. Zhang, Z. G. Hu, J. H. Chu, *ACS Appl. Mater. Interfaces* **2020**, *12*, 18674.
- [25] J. Yao, F. Chen, J. Li, J. Du, D. Wu, Y. Tian, C. Zhang, J. Yang, X. Li, P. Lin, *J. Mater. Chem. C* **2021**, *9*, 13123.
- [26] Z. Zhang, B. Zhao, D. Shen, Q. Tao, B. Li, R. Wu, B. Li, X. Yang, J. Li, R. Song, *Small Struct.* **2021**, *2*, 2100028.
- [27] M. M. Tavakoli, S. M. Zakeeruddin, M. Gratzel, Z. Fan, *Adv. Mater.* **2018**, *30*, 1705998.
- [28] J. K. Qin, G. Qiu, W. He, J. Jian, M. W. Si, Y. Q. Duan, A. Charnas, D. Y. Zemlyanov, H. Y. Wang, W. Z. Shao, L. Zhen, C. Y. Xu, P. D. Ye, *Adv. Funct. Mater.* **2018**, *28*, 1806254.
- [29] C. Y. Tan, S. Q. Yin, J. W. Chen, Y. Lu, W. S. Wei, H. F. Du, K. L. Liu, F. K. Wang, T. Y. Zhai, L. Li, *ACS Nano* **2021**, *15*, 8328.
- [30] L. X. Han, M. M. Yang, P. T. Wen, W. Gao, N. J. Huo, J. B. Li, *Nanoscale Adv.* **2021**, *3*, 2657.
- [31] J. H. Kim, M. R. Bergren, J. C. Park, S. Adhikari, M. Lorke, T. Frauenheim, D. H. Choe, B. Kim, H. Choi, T. Gregorkiewicz, Y. H. Lee, *Nat. Commun.* **2019**, *10*, 5488.
- [32] a) H. Y. Wang, Z. X. Li, D. Y. Li, X. Xu, P. Chen, L. J. Pi, X. Zhou, T. Y. Zhai, *Adv. Funct. Mater.* **2021**, *31*, 2106105; b) P. Luo, F. Zhuge, F. Wang, L. Lian, K. Liu, J. Zhang, T. Zhai, *ACS Nano* **2019**, *13*, 9028.
- [33] M. Buscema, D. J. Groenendijk, S. I. Blanter, G. A. Steele, H. S. J. van der Zant, A. Castellanos-Gomez, *Nano Lett.* **2014**, *14*, 3347.
- [34] L. H. Zeng, S. H. Lin, Z. J. Li, Z. X. Zhang, T. F. Zhang, C. Xie, C. H. Mak, Y. Chai, S. P. Lau, L. B. Luo, Y. H. Tsang, *Adv. Funct. Mater.* **2018**, *28*, 1705970.
- [35] N. N. Li, Y. Wen, R. Q. Cheng, L. Yin, F. Wang, J. Li, T. A. Shifa, L. P. Feng, Z. X. Wang, J. He, *Appl. Phys. Lett.* **2019**, *114*, 103501.
- [36] X. Zhou, X. Z. Hu, J. Yu, S. Y. Liu, Z. W. Shu, Q. Zhang, H. Q. Li, Y. Ma, H. Xu, T. Y. Zhai, *Adv. Funct. Mater.* **2018**, *28*, 1706587.
- [37] H.-G. Park, *J. Korean Phys. Soc.* **2018**, *73*, 218.
- [38] a) T. Tong, Y. F. Chen, S. C. Qin, W. S. Li, J. R. Zhang, C. H. Zhu, C. C. Zhang, X. Yuan, X. Q. Chen, Z. H. Nie, X. R. Wang, W. D. Hu, F. Q. Wang, W. Q. Liu, P. Wang, X. F. Wang, R. Zhang, Y. B. Xu, *Adv. Funct. Mater.* **2019**, *29*, 1905806; b) C. Y. Hong, Y. Tao, A. M. Nie, M. H. Zhang, N. Wang, R. P. Li, J. Q. Huang, Y. Q. Huang, X. M. Ren, Y. C. Cheng, X. L. Liu, *ACS Nano* **2020**, *14*, 16803.
- [39] a) J. B. Yin, Z. J. Tan, H. Hong, J. X. Wu, H. T. Yuan, Y. J. Liu, C. Chen, C. W. Tan, F. R. Yao, T. R. Li, Y. L. Chen, Z. F. Liu, K. H. Liu, H. L. Peng, *Nat. Commun.* **2019**, *10*, 3311; b) M. Peng, R. Xie, Z. Wang, P. Wang, F. Wang, H. Ge, Y. Wang, F. Zhong, P. Wu, J. Ye, *Sci. Adv.* **2021**, *7*, 7358.
- [40] C. Chen, M. X. Wang, J. X. Wu, H. X. Fu, H. F. Yang, Z. Tian, T. Tu, H. Peng, Y. Sun, X. Xu, J. Jiang, N. B. M. Schroter, Y. W. Li, D. Pei, S. Liu, S. A. Ekahana, H. T. Yuan, J. M. Xue, G. Li, J. F. Jia, Z. K. Liu, B. H. Yan, H. L. Peng, Y. L. Chen, *Sci. Adv.* **2018**, *4*.
- [41] Y. C. Du, G. Qiu, Y. X. Wang, M. W. Si, X. F. Xu, W. Z. Wu, P. D. D. Ye, *Nano Lett.* **2017**, *17*, 3965.
- [42] a) L. Li, W. K. Wang, L. Gan, N. Zhou, X. D. Zhu, Q. Zhang, H. Q. Li, M. L. Tian, T. Y. Zhai, *Adv. Funct. Mater.* **2016**, *26*, 8281; b) G. H. Shin, C. Park, K. J. Lee, H. J. Jin, S. Y. Choi, *Nano Lett.* **2020**, *20*, 5741.
- [43] Y. Xin, X. Wang, Z. Chen, D. Weller, Y. Wang, L. Shi, X. Ma, C. Ding, W. Li, S. Guo, *ACS Appl. Mater. Interfaces* **2020**, *12*, 15406.
- [44] B. N. Zheng, Z. H. Wu, F. Guo, R. Ding, J. F. Mao, M. H. Xie, S. P. Lau, J. H. Hao, *Adv. Opt. Mater.* **2021**, *9*, 2101052.
- [45] F. L. Qin, F. Gao, M. J. Dai, Y. X. Hu, M. M. Yu, L. F. Wang, W. Feng, B. Li, P. A. Hu, *ACS Appl. Mater. Interfaces* **2020**, *12*, 37313.
- [46] Z. Lu, Y. Xu, Y. Yu, K. Xu, J. Mao, G. Xu, Y. Ma, D. Wu, J. Jie, *Adv. Funct. Mater.* **2020**, *30*, 1907951.
- [47] Y. Zhang, W. X. Xu, X. J. Xu, W. Yang, S. Y. Li, J. X. Chen, X. S. Fang, *Nanoscale Horiz.* **2019**, *4*, 452.
- [48] H. Shang, H. Chen, M. Dai, Y. Hu, F. Gao, H. Yang, B. Xu, S. Zhang, B. Tan, X. Zhang, *Nanoscale Horiz.* **2020**, *5*, 564.
- [49] W. D. Song, J. X. Chen, Z. L. Li, X. S. Fang, *Adv. Mater.* **2021**, *33*, 2101059.
- [50] Q. X. Zhao, F. Gao, H. Y. Chen, W. Gao, M. J. Xia, Y. Pan, H. Y. Shi, S. C. Su, X. S. Fang, J. B. Li, *Mater. Horiz.* **2021**, *8*, 3113.
- [51] H. M. Shang, H. Y. Chen, M. J. Dai, Y. X. Hu, F. Gao, H. H. Yang, B. Xu, S. C. Zhang, B. Y. Tan, X. Zhang, P. A. Hu, *Nanoscale Horiz.* **2020**, *5*, 564.
- [52] V. Klee, E. Preciado, D. Barroso, A. E. Nguyen, C. Lee, K. J. Erickson, M. Triplett, B. Davis, I.-H. Lu, S. Bobek, *Nano Lett.* **2015**, *15*, 2612.
- [53] a) C. Guthmann, C. Hermann, J. Thuillier, *Phys. Status Solidi A* **1970**, *3*, 365; b) V. A. Vis, *J. Appl. Phys.* **1964**, *35*, 360.
- [54] W. J. Chen, U. Khan, S. M. Feng, B. F. Ding, X. M. Xu, B. L. Liu, *Adv. Funct. Mater.* **2020**, *30*, 2004960.